



Article

High-Resolution Remotely Sensed Evidence Shows Solar Thermal Power Plant Increases Grassland Growth on the Tibetan Plateau

Naijing Liu ^{1,2} , Huaiwu Peng ^{1,*} , Zhenshi Zhang ¹, Yujin Li ¹, Kai Zhang ³, Yuehan Guo ¹, Yuzheng Cui ⁴, Yingsha Jiang ¹, Wenxiang Gao ¹ and Donghai Wu ⁵

- ¹ POWERCHINA Northwest Engineering Corporation Limited, Xi'an 710065, China; liunj@mail.bnu.edu.cn (N.L.); zzs-483@nwh.cn (Z.Z.); liyuj@nwh.cn (Y.L.); guoyh@nwh.cn (Y.G.); jiangyings@nwh.cn (Y.J.); xby03480@powerchina.cn (W.G.)
- ² State Key Joint Laboratory of Environmental Simulation and Pollution Control, School of Environment, Beijing Normal University, Beijing 100875, China
- ³ Department of Geography and Resource Management, The Chinese University of Hong Kong, Hong Kong 999077, China; kaizhang001@cuhk.edu.hk
- ⁴ School of Geography and Tourism, Shaanxi Normal University, Xi'an 710119, China; yuzheng-cui@snnu.edu.cn
- ⁵ Key Laboratory of Vegetation Restoration and Management of Degraded Ecosystems, and Guangdong Provincial Key Laboratory of Applied Botany, South China Botanical Garden, Chinese Academy of Sciences, Guangzhou 510650, China; donghaiwu@srbg.ac.cn
- * Correspondence: penghuaiw@nwh.cn

Abstract: Solar energy plays a crucial role in mitigating greenhouse gas emissions in the context of global climate change. However, its deployment for green electricity generation can significantly influence regional climate and vegetation dynamics. While prior studies have examined the impacts of solar power plants on vegetation, the accuracy of these assessments has often been constrained by the availability of publicly accessible multispectral, high-resolution remotely sensed imagery. Given the abundant solar energy resources and the ecological significance of the Tibetan Plateau, a thorough evaluation of the vegetation effects associated with solar power installations is warranted. In this study, we utilize sub-meter resolution imagery from the GF-2 satellite to reconstruct the fractional vegetation cover (FVC) at the Gonghe solar thermal power plant through image classification, in situ sampling, and sliding window techniques. We then quantify the plant's impact on FVC by comparing data from the pre-installation and post-installation periods. Our findings indicate that the Gonghe solar thermal power plant is associated with a 0.02 increase in FVC compared to a surrounding control region ($p < 0.05$), representing a 12.5% increase relative to the pre-installation period. Notably, the enhancement in FVC is more pronounced in the outer ring areas than near the central tower. The observed enhancement in vegetation growth at the Gonghe plant suggests potential ecological and carbon storage benefits resulting from solar power plant establishment on the Tibetan Plateau. These findings underscore the necessity of evaluating the climate and ecological impacts of renewable energy facilities during the planning and design phases to ensure a harmonious balance between clean energy development and local ecological integrity.

Keywords: fractional vegetation cover; land cover; solar thermal power plant; Tibetan Plateau



Citation: Liu, N.; Peng, H.; Zhang, Z.; Li, Y.; Zhang, K.; Guo, Y.; Cui, Y.; Jiang, Y.; Gao, W.; Wu, D. High-Resolution Remotely Sensed Evidence Shows Solar Thermal Power Plant Increases Grassland Growth on the Tibetan Plateau. *Remote Sens.* **2024**, *16*, 4266. <https://doi.org/10.3390/rs16224266>

Academic Editor: Brenden E. McNeil

Received: 27 September 2024

Revised: 5 November 2024

Accepted: 13 November 2024

Published: 15 November 2024



Copyright: © 2024 by the authors. Licensee MDPI, Basel, Switzerland. This article is an open access article distributed under the terms and conditions of the Creative Commons Attribution (CC BY) license (<https://creativecommons.org/licenses/by/4.0/>).

1. Introduction

Renewable energy is pivotal in mitigating the climate change effects associated with fossil fuel combustion [1]. As a significant component of the renewable energy landscape, global installed solar power capacity reached 1500 gigawatts in 2023. Leading the world in solar energy deployment, China accounted for 45% of the global installed capacity in 2023, reflecting a growth rate of 70% compared to the previous year [2]. This trend is expected to

continue in alignment with China's goals for carbon peaking and neutrality [3,4]. However, solar photovoltaic systems generate electricity primarily during daylight hours when solar radiation is abundant, resulting in an imbalance in electricity output that complicates grid management [5]. As a supplementary for solar photovoltaic systems, solar thermal power plants integrate both electricity generation and energy storage, thereby contributing to a more stable electricity output curve, which is increasingly recognized as a critical component of future renewable energy development [6,7]. In 2023, the global installed capacity of concentrated solar thermal power surpassed 7 gigawatts, reflecting an 11% increase over the previous year [8].

Despite their potential to produce clean electricity, solar power plants can exert localized climate and ecological impacts [9–11]. Although the energy conversion processes differ between solar photovoltaic and solar thermal systems, both technologies intercept or reflect solar radiation and alter surface roughness, leading to similar climatic and ecological consequences [12–14]. During the day, these systems provide shade to the ground and reduce incoming solar radiation, potentially lowering surface temperatures [15–17]. Conversely, at night, they may restrict upward longwave radiation, potentially inducing a warming effect on the surface [18,19]. Unlike photovoltaic panels, which convert solar radiation into electricity while generating heat [20], the reflecting mirrors of solar thermal power plants primarily reflect radiation, resulting in lower surrounding air temperatures compared to photovoltaic installations. Previous research also documented the influence of precipitation and near-surface wind speed associated with solar photovoltaic installations [12,21]. Such effects may either enhance or inhibit vegetation growth, depending on the local climatic and land cover conditions [18,22–25].

While existing studies have explored the climatic and vegetative impacts of solar power plants, several areas warrant further investigation. First, analyses of vegetation impacts derived from satellite remote sensing have typically utilized imagery from Sentinel-2 (10 m spatial resolution), Landsat (30 m spatial resolution), or other products with coarser resolutions [18,24,25]. Given that the prevailing width of solar photovoltaic panel arrays is 4–5 m, with inter-array gaps of 4–6 m in mid-latitude regions, the spatial resolution of 10 m or coarser often mixes information from both the solar panels and the surrounding land surface, potentially introducing uncertainty into assessments of vegetation dynamics [26,27]. Second, considering the high ecological sensitivity and carbon storage significance of the Tibetan Plateau, coupled with its abundant solar energy resources, it is imperative to evaluate the vegetation impacts associated with solar power installations in this region [28,29]. Additionally, the ecological implications of solar thermal power plants, which serve both electricity generation and energy storage functions, remain underexplored.

In this study, we assess the impact of the Gonghe solar thermal power plant on fractional vegetation cover (FVC) using GF-2 sub-meter satellite remote sensing imagery with a spatial resolution of 0.8 m. By employing soft voting classification to identify pixels covered by the power plant's reflecting mirrors, we reconstruct the FVC beneath these mirrors using in situ samples and a sliding window approach. The impacts of the Gonghe solar thermal power plant on FVC are then evaluated through a comparison of data from the pre-installation and post-installation periods.

2. Materials and Methods

2.1. Study Area

Gonghe County is characterized by abundant solar resources, with annual total solar radiation exceeding 6000 megajoules m^{-2} in the study area [30]. This abundant resource has facilitated the establishment of over 2.2 gigawatts of installed solar energy capacity in the surrounding region [23]. The Gonghe solar thermal power plant is situated in Gonghe County, in the northeastern region of the Tibetan Plateau, featuring an installed capacity of 50 megawatts, and was constructed in 2018. This facility harnesses heat energy through more than 30,000 reflecting mirrors, with a central solar power tower, and utilizes molten salts for energy storage, allowing for a maximum storage duration of six hours. Geograph-

ically, the Gonghe solar thermal power plant is located at 100.6°E longitude and 36.1°N latitude, at an elevation of 2880 m. The average annual precipitation is 303 mm, and the mean annual air temperature is 4°C , characterizing the area as semi-arid with relatively low temperatures [23]. The underlying terrain consists of degraded grassland, predominantly featuring grasses and shrubs, with an average normalized difference vegetation index (NDVI) ranging from 0.1 to 0.3 across the study area [23]. To assess the impact of the Gonghe solar thermal power plant on fractional vegetation cover (ΔFVC), a control area was established within a 0 to 300 m radius surrounding the facility, primarily consisting of grassland (Figure 1). This control area was selected due to its similar climatic and vegetative characteristics to those of the power plant, ensuring that any observed differences in FVC can be attributed primarily to the solar installation and operation [18,24]. To mitigate the influence of buildings and impervious surfaces, we defined a study area encompassing the mirror field, which includes the predominant land cover types of grassland, bare land, and reflecting mirrors.

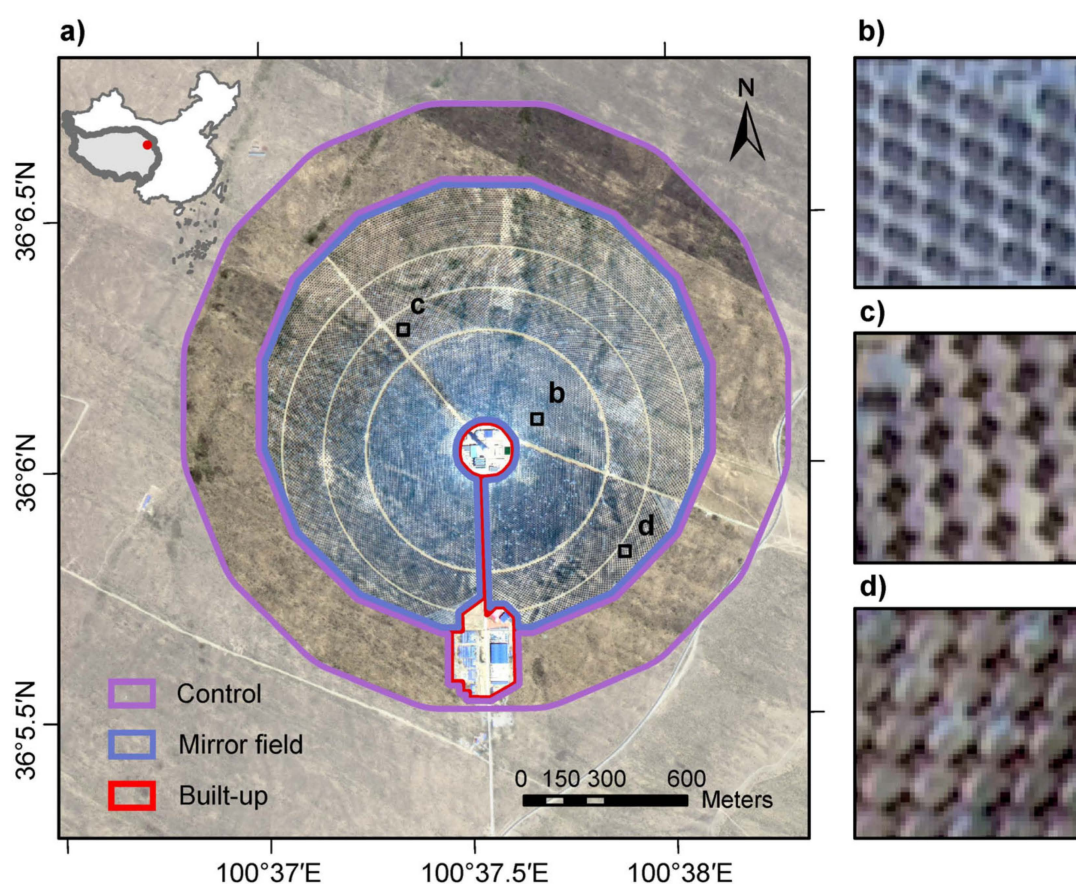


Figure 1. Study area. (a) Geolocation and true color composite image of the Gonghe solar thermal power plant, captured by GF-2 with a spatial resolution of 0.8 m. Detailed representations of the Gonghe solar thermal power plant are provided in subfigures (b–d), with their respective locations indicated within the main figure (a).

2.2. Data

To reconstruct the FVC of the Gonghe solar thermal power plant, this study utilizes GF-2 sub-meter satellite remote sensing imagery [31,32]. Given that the plant was constructed in 2018, it is necessary to obtain imagery from both before and after this construction period to accurately assess the ΔFVC . After filtering the images based on vegetation phenology and cloud cover, we selected two images captured during the peak growing seasons of 2017 and 2020. The image IDs are GF2_PMS2_E100.7_N36.1_20170731_L1A0002517445 and GF2_PMS1_E100.7_N36.2_20200729_L1A0004956637. The Level 1A images under-

went several preprocessing steps, including radiometric calibration, FLAASH atmospheric correction [33], geometric correction, and orthorectification. The initial spatial resolution of the GF-2 imagery is 0.8 m for panchromatic bands and 3.2 m for multispectral bands. Image fusion was performed using the NNDiffuse Pan Sharpening algorithm to generate 0.8 m multispectral surface reflectance bands, which include blue, green, red, and near-infrared [34]. All preprocessing procedures were conducted using ENVI 5.4 software.

Given the presence of over 30,000 reflecting mirrors at the Gonghe solar thermal power plant, it is essential to quantify the FVC beneath these mirrors to reconstruct the overall FVC for the facility. We collected in situ sample pairs of FVC measurements from areas directly under the mirrors and from adjacent inter-mirror spaces. These sample pairs were documented using a smartphone camera to capture RGB images in July 2024, with the geolocations recorded using a portable GPS receiver. The images were taken perpendicularly to the ground, and the edges were cropped to mitigate camera distortion, ensuring their suitability for subsequent FVC extraction. In total, 174 sample pairs were selected, with their locations depicted in Figure S1.

To investigate the mechanisms underlying changes in FVC at the Gonghe solar thermal power plant, we utilized monthly aggregated data on precipitation and potential evaporation from the European Centre for Medium-Range Weather Forecasts Reanalysis v5 Land (ERA5-Land) spanning the years 2010 to 2020, which has a spatial resolution of 9 km [35]. The ERA5-Land data are obtained and calculated via Google Earth Engine (GEE) [36].

2.3. Methods

To evaluate the Δ FVC of the Gonghe solar thermal power plant, we employed a three-step methodology. First, we recognized the pixels obscured by the reflecting mirrors by extracting mirror pixels through land cover classification, utilizing vegetation indices and multispectral surface reflectance data from GF-2 imagery. Second, we applied a 3×3 sliding window kernel to interpolate the FVC values under the mirrors, incorporating data from land cover classification, GF-2-derived FVC, and the FVC ratios derived from in situ sample pairs collected from areas beneath and between the mirrors. Finally, the impact on FVC was quantified by calculating the difference between the reconstructed FVC for the post-installation year of 2020 and the GF-2 FVC for the pre-installation year of 2017 (see Figure 2).

2.3.1. Reflecting Mirror Extraction Algorithm

To accurately reconstruct the FVC of the Gonghe solar thermal power plant, it is essential to extract the pixels corresponding to the mirrors in order to update the GF-2 FVC pixel values appropriately. In pursuit of this objective, we categorized the land cover within the power plant into three distinct types: grassland, mirror, and bare land/impervious surfaces, based on the landscape characteristics and spectral information provided by GF-2 data.

In this study, we selected a total of 550 training samples, supplemented by an additional 200 validation samples. The land cover classifications for these samples were determined through visual interpretation of GF-2 true color and false color composite images (comprising near-infrared, red, and green bands). The training dataset consists of 265 grassland samples, 188 mirror samples, and 97 samples representing bare land and impervious surfaces. The validation dataset includes 106 grassland samples, 62 mirror samples, and 32 samples of bare land and impervious surfaces. The specific locations of these samples are illustrated in Figure S2.

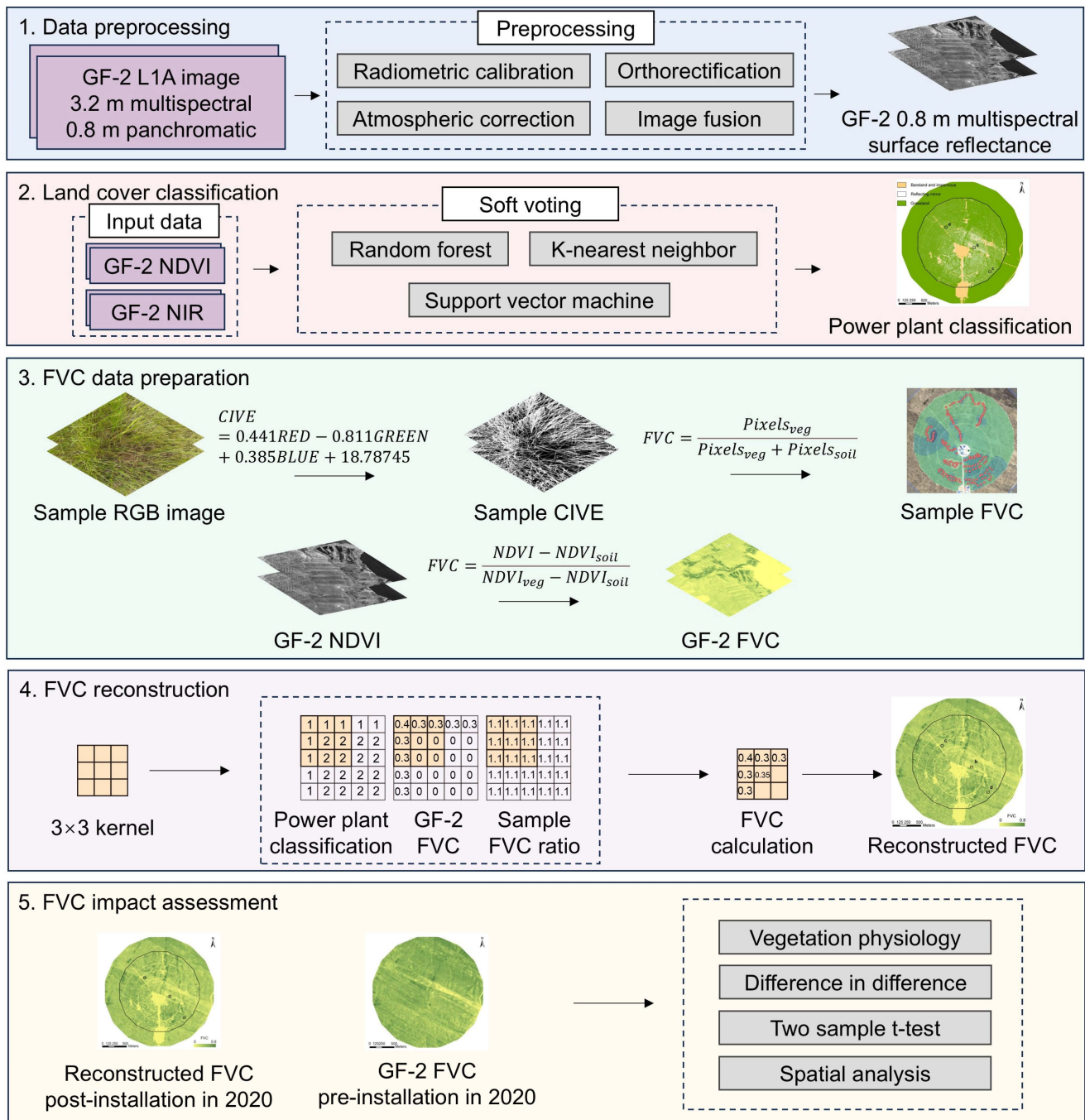


Figure 2. Workflow of the study. The primary steps include data preprocessing, land cover classification, fractional vegetation cover (FVC) data preparation, FVC reconstruction, and assessment of FVC impacts within the Gonghe solar thermal power plant.

To enhance the robustness of our classification results, we employed a soft voting classifier, which integrates multiple individual sub-classifiers and derives classification outcomes based on a synthesis of the classification probabilities from these sub-classifiers [37]. In this study, the soft voting classifier comprises three distinct sub-classifiers: random forest, support vector machine, and k-nearest neighbor. The random forest classifier operates by constructing multiple decision trees, with each tree built using a random subset of the dataset and evaluating a random subset of features at each node [38]. The support vector machine classifier identifies the optimal hyperplane within an N-dimensional space, effectively separating data points belonging to different classes in the feature space, while

maximizing the margin between the nearest points of the respective classes [39]. The k-nearest neighbor algorithm determines the class or value of a data point by identifying the k-nearest neighbors based on distance metrics, then assigning the class based on a majority vote or averaging the values of these neighbors [40].

Following an evaluation of the significance of each multispectral band and the NDVI, as defined in Equation (1), we have selected NDVI along with the reflectance of the near-infrared band for inclusion in our classification analysis.

$$\text{NDVI} = \frac{\text{NIR} - \text{RED}}{\text{NIR} + \text{RED}} \quad (1)$$

where NIR and RED represent the surface reflectance of the near-infrared and red bands from the GF-2 imagery. The soft voting classifier was implemented in Python 3.10 utilizing the scikit-learn package (version 1.2.2) [41]. After evaluating the classifier's performance, we established the parameters for the sub-classifiers, as detailed in Table 1. Following validation through a confusion matrix, f1_score, and kappa coefficient, we classified the post-installation GF-2 imagery from 2020 for the Gonghe solar thermal power plant.

Table 1. The parameter set for the soft voting classifier utilized in this study. The abbreviations RF, SVM, and KNN refer to the random forest, support vector machine, and k-nearest neighbor sub-classifiers, respectively.

Parameter	Value	Explanation
n_estimators (RF)	20	The number of trees in the forest
max_depth (RF)	13	The maximum depth of the tree
min_samples_split (RF)	50	The minimum number of samples required to split an internal node
min_samples_leaf (RF)	10	The minimum number of samples required to be at a leaf node
max_features (RF)	7	The number of features to consider when looking for the best split
Probability (SVM)	True	Whether to enable probability estimates
n_neighbors (KNN)	13	Number of neighbors to use by default for k-neighbors queries

2.3.2. FVC Reconstruction

In this study, we incorporate three critical datasets into the reconstruction methodology for FVC. Firstly, we utilize the land cover classification results for the Gonghe solar thermal power plant from 2020, which serve to identify the mirror pixels requiring reconstruction. Secondly, we consider the FVC ratio derived from sample pairs collected from areas beneath and between the mirrors, which provides insight into the FVC coefficients of mirror-covered pixels in relation to their surrounding uncovered counterparts. Lastly, we reference the FVC for the Gonghe solar thermal power plant as recorded in 2020.

The land cover classification results were presented in Section 2.3.1, following which we proceeded to calculate the FVC ratio. We collected 174 sample pairs within the Gonghe solar thermal power plant using a smartphone camera, necessitating the computation of FVC based exclusively on RGB bands. Numerous methods exist for calculating vegetation indices from RGB imagery [42,43]; however, after evaluating their respective performances, we selected the color index of vegetation extraction (CIVE) for this study, defined as follows

$$\text{CIVE} = 0.441\text{RED} - 0.811\text{GREEN} + 0.385\text{BLUE} + 18.78745 \quad (2)$$

where RED, GREEN, and BLUE correspond to the respective channels of the RGB image. The CIVE is then binarized to distinguish between vegetation and soil pixels. The FVC for the RGB image is calculated using the formula:

$$\text{FVC} = \frac{\text{Pixels}_{\text{veg}}}{\text{Pixels}_{\text{veg}} + \text{Pixels}_{\text{soil}}} \quad (3)$$

where $\text{Pixels}_{\text{veg}}$ and $\text{Pixels}_{\text{soil}}$ denote the number of pixels in the binarized image corresponding to vegetation and soil, respectively. The FVC ratio is subsequently computed by dividing the FVC beneath the mirrors by the FVC between the mirrors for each sample pair. This ratio is then interpolated across the entire power plant using the inverse distance weighting (IDW) method [44]. The difference between the FVC beneath the mirrors by the FVC between the mirrors is illustrated as δFVC in the following texts.

The GF-2 FVC is computed based on the NDVI derived from GF-2 imagery, using the following formula:

$$\text{FVC} = \frac{\text{NDVI} - \text{NDVI}_{\text{soil}}}{\text{NDVI}_{\text{veg}} - \text{NDVI}_{\text{soil}}} \quad (4)$$

where NDVI represents the pixel values from the GF-2 NDVI image, and NDVI_{veg} and $\text{NDVI}_{\text{soil}}$ are the NDVI values corresponding to fully vegetated and bare soil areas, respectively. To assess the accuracy of the GF-2 FVC, we conducted in situ measurements utilizing a smartphone camera in conjunction with the FVC definition provided in Equation (3). The evaluation results indicate a high degree of accuracy for the GF-2 FVC, with a coefficient of determination (R^2) of 0.92 and a root mean square error (RMSE) of 0.02 when compared to the in situ measurements (Figure S3). The high accuracy supports our analysis of the impacts of the Gonghe solar thermal power plant on FVC.

To reconstruct the FVC of the mirror pixels, we employ a 3×3 sliding window kernel to traverse the land cover classification results from the Gonghe solar thermal power plant in 2020. Initially, if the central pixel of the 3×3 kernel corresponds to a mirror pixel, we utilize the remaining eight pixels within the kernel to calculate the FVC for the central pixel. Next, we filter these eight pixels based on their land cover types, excluding any mirror types from the calculation. The weights of the remaining pixels are computed using inverse distance weighting:

$$w_i = \frac{\frac{1}{d_i}}{\sum_{i=1}^n \frac{1}{d_i}} \quad (5)$$

where w_i is the weight assigned to each remaining pixel, d_i is the distance from the remaining pixels to the central pixel, and n is the total number of remaining pixels. The FVC for the central pixel is then calculated as follows:

$$\text{FVC}_c = \sum_{i=1}^n w_i \times \text{FVC}_i \times r \quad (6)$$

where FVC_c represents the calculated FVC for the central pixel, FVC_i denotes the GF-2 FVC values of each remaining pixel, and r is the FVC ratio derived from the sample pairs. Finally, the land cover classification of the central pixel is altered from “mirror” to “reconstructed”. Upon completion of this traversal across all pixels within the land cover classification results, we successfully reconstructed the FVC for the mirror pixels of the Gonghe solar thermal power plant as recorded in 2020.

2.3.3. Assessment of the FVC Impact

The ΔFVC is derived using the “difference in differences” approach, which assesses the FVC variations between the power plant area and a corresponding control region during two distinct periods: the pre-installation phase in 2017 and the post-installation phase in 2020 [45,46]. This is expressed mathematically as:

$$\text{FVCDIF} = \text{FVC}_{2020} - \text{FVC}_{2017} \quad (7)$$

$$\Delta\text{FVC} = \overline{\text{FVCDIF}_{\text{solar}}} - \overline{\text{FVCDIF}_{\text{control}}} \quad (8)$$

where FVC_{2020} represents the reconstructed FVC for the year 2020, FVC_{2017} denotes the GF-2 FVC for 2017, FVCDIF signifies the difference in FVC between FVC_{2020} and FVC_{2017} , and $\overline{\text{FVCDIF}_{\text{solar}}}$ and $\overline{\text{FVCDIF}_{\text{control}}}$ are the mean FVC differences for the solar plant and the

surrounding control regions, respectively. The statistical significance of Δ FVC is assessed using a two-sample *t*-test. To assess how the difference in FVC varies with distance from the central tower and the overall power plant, we calculated the average FVC differences within the concentric ring regions of the power plant, as well as at 100 m intervals extending from 0 to 500 m beyond its boundaries.

3. Results

3.1. Reflecting Mirror Extraction

In this study, we utilized 550 training samples and 200 validation samples to classify land cover within the Gonghe solar thermal power plant for the year 2020. The performance of the soft voting classifier is illustrated in the confusion matrices presented in Figure 3. The training accuracy achieved by the soft voting classifier was 96%, with a corresponding validation accuracy of 96%. Additionally, the classifier yielded an *f1_score* of 0.95 and a kappa coefficient of 0.93, indicating a robust performance in the classification task associated with the Gonghe solar thermal power plant.

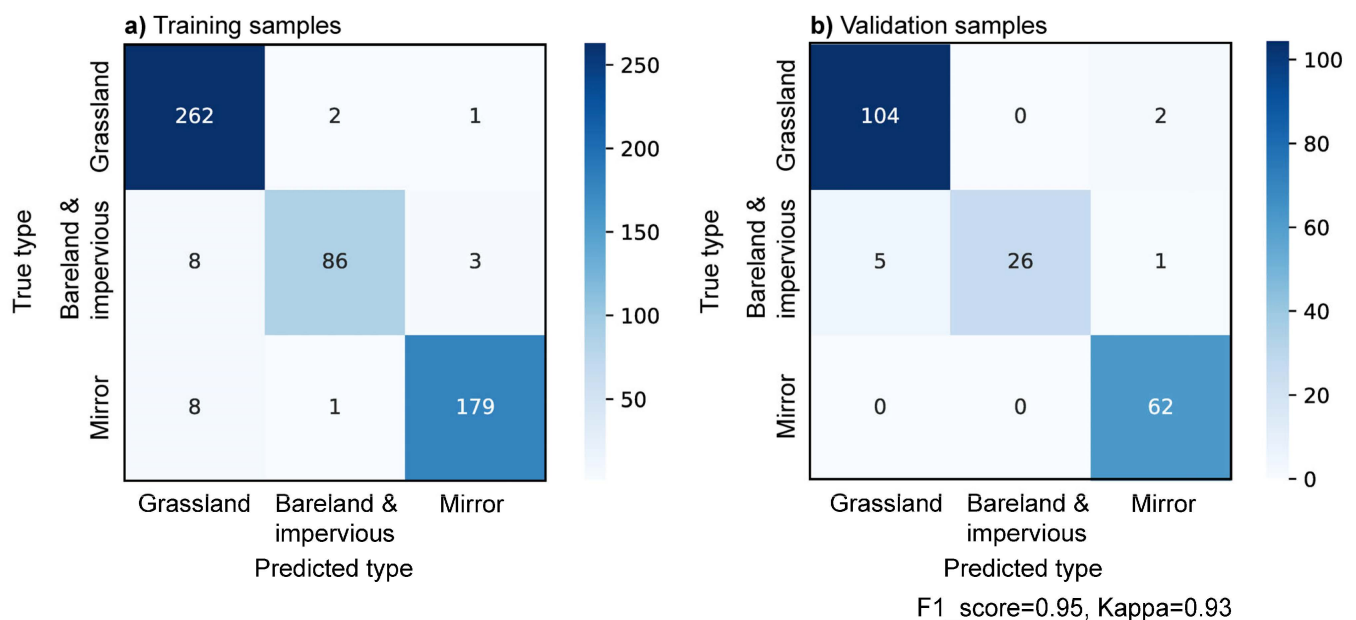


Figure 3. Confusion matrices of soft voting classification in this study. Subfigure (a) illustrates the confusion matrix for the training samples, while subfigure (b) presents the confusion matrix for the validation samples. The *f1_score* and the kappa value for the validation samples are detailed in the accompanying text.

Following the assessment of the soft voting classifier's performance on the Gonghe solar thermal power plant, we proceeded to apply it to the entire image dataset. As depicted in Figure 4, the classification results effectively identify and characterize land cover types, including grassland, reflecting mirrors, together with bare land and impervious surfaces. Specifically, these three categories—grassland, reflecting mirrors, and bare land and impervious surfaces—account for 76.5%, 14.7%, and 8.8% of the total pixels within the power plant, respectively. Notably, a comparison of Figure 4b–d with Figure 1b–d demonstrates that the soft voting classifier accurately extracts reflecting mirrors across a range of rotational and pitch orientations.

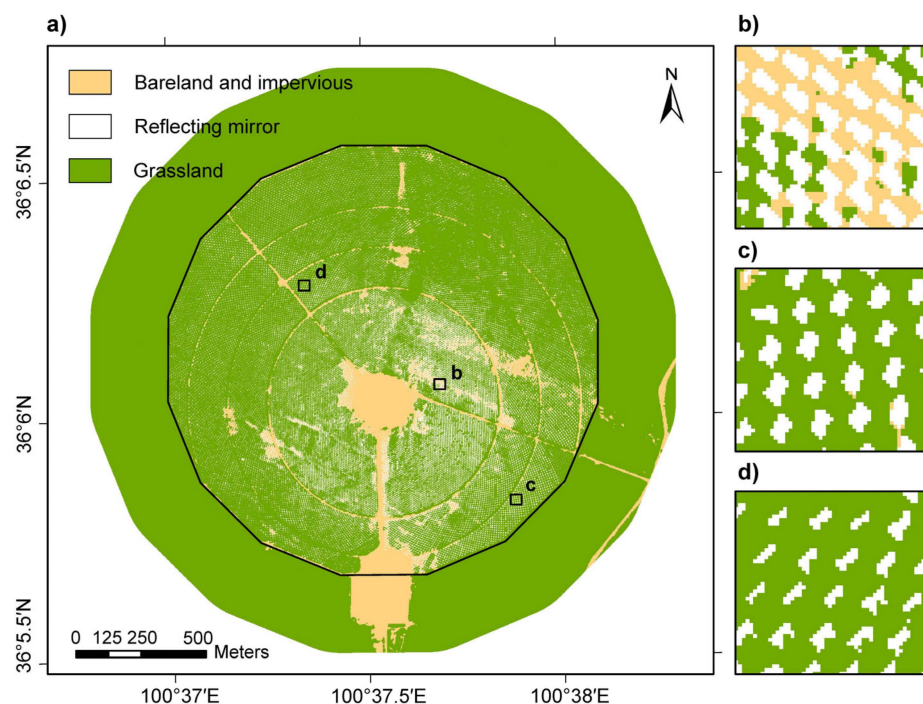


Figure 4. Soft voting classification results of the Gonghe solar thermal power plant. The classification results are detailed in subfigures (b–d), with their respective positions indicated in the main figure (a). Areas classified as bare land and impervious surfaces are represented in brown, reflecting mirrors in white, and grassland in green.

3.2. Reconstruction of FVC

We collected 174 sample pairs to assess the FVC ratio beneath reflecting mirror surfaces compared to adjacent uncovered areas. The average FVC between the mirrors was measured at 0.16, while the mean FVC beneath the mirrors was found to be 0.21. Our in situ sampling indicates that the reflecting mirrors at the Gonghe solar thermal power plant enhanced δFVC by 0.05, achieving statistical significance at $p < 0.001$. The average FVC ratio between the areas under the mirrors and those between them was calculated to be 1.36, with the spatial distribution illustrated in Figure S4a. Figure S4d–e presents the RGB images of the sample pairs alongside the binarized FVC images.

The FVC was reconstructed using a 3×3 kernel in conjunction with classification data, GF-2 FVC, and the in situ sample ratio from the Gonghe solar thermal power plant. As depicted spatially in Figure 5a, the mean reconstructed FVC for both the power plant and the surrounding control regions was determined to be 0.21. Notably, the reconstructed FVC was slightly higher beneath the mirrors than in the adjacent uncovered areas, reflecting the average in situ sample ratio of 1.36 observed between these two regions.

3.3. Impacts of Solar Thermal Station on FVC

By calculating the difference in FVC between the post-installation period of 2020 and the pre-installation period of 2017, we can determine the ΔFVC associated with the Gonghe solar thermal power plant. This is achieved by comparing the FVC differences within the plant itself and in the surrounding control regions. Focusing solely on the natural surfaces impacted by the installation, which are expected to recover over time in response to climatic conditions and human management, ΔFVC between the mirror field and control region indicates a notable increase in FVC attributable to the power plant, measured at 0.02, with a significance level of $p < 0.05$, as shown in Figure 6. To mitigate the uncertainties arising from the temporal mismatch between in situ measurements and GF-2 image capture, we also calculated the ΔFVC specifically for grassland pixels to eliminate potential influences

associated with the year gap. The results indicate that the Gonghe solar thermal power plant contributes to a ΔFVC of 0.027, with a significance level of $p < 0.01$ (Figure S5).

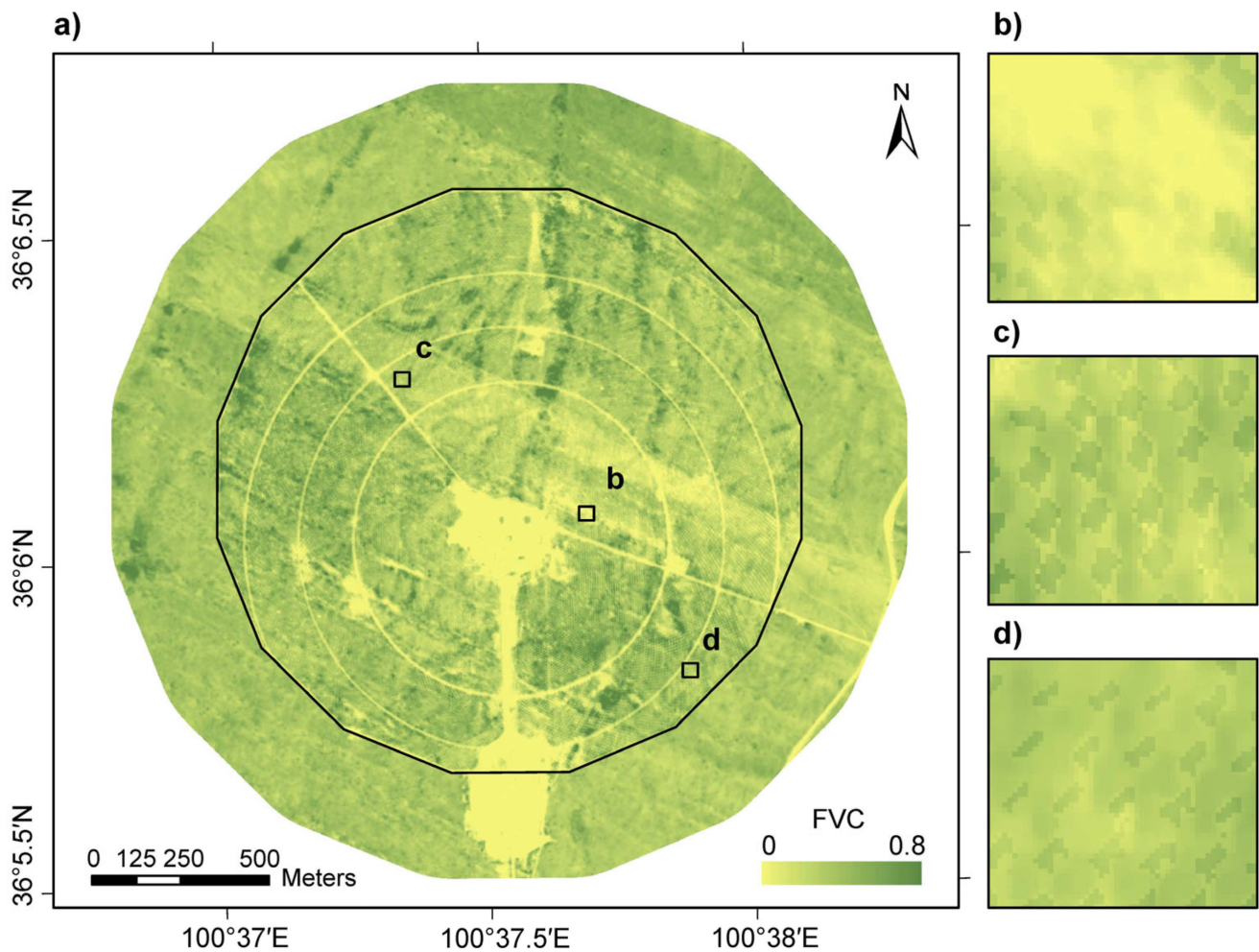


Figure 5. FVC reconstruction results of the Gonghe solar thermal power plant in 2020. The detailed results of the FVC reconstruction are presented in subfigures (b–d), with their respective locations indicated in the main figure (a).

It is of considerable interest to investigate whether the FVC difference varies with distance from the central tower of the power plant and to ascertain the broader impacts of the power plant on its surrounding areas. To address this, we divided the power plant into four rings, with an extra five rings extending every 100 m from the power plant border out to 500 m, as illustrated in Figure 7a. The average FVC differences were calculated for each ring, revealing that the FVC difference is notably lower in the innermost ring surrounding the central tower compared to the outer rings. This trend is consistent with the spatial representation illustrated in Figure 6a. However, an analysis of the outer rings does not reveal a discernible trend in FVC differences, suggesting that the spillover effects of the Gonghe solar thermal power plant on surrounding vegetation are minimal. Furthermore, the standard deviation of FVC differences within the power plant, at 0.10, is significantly greater than that of the outer rings, which stand at 0.05.

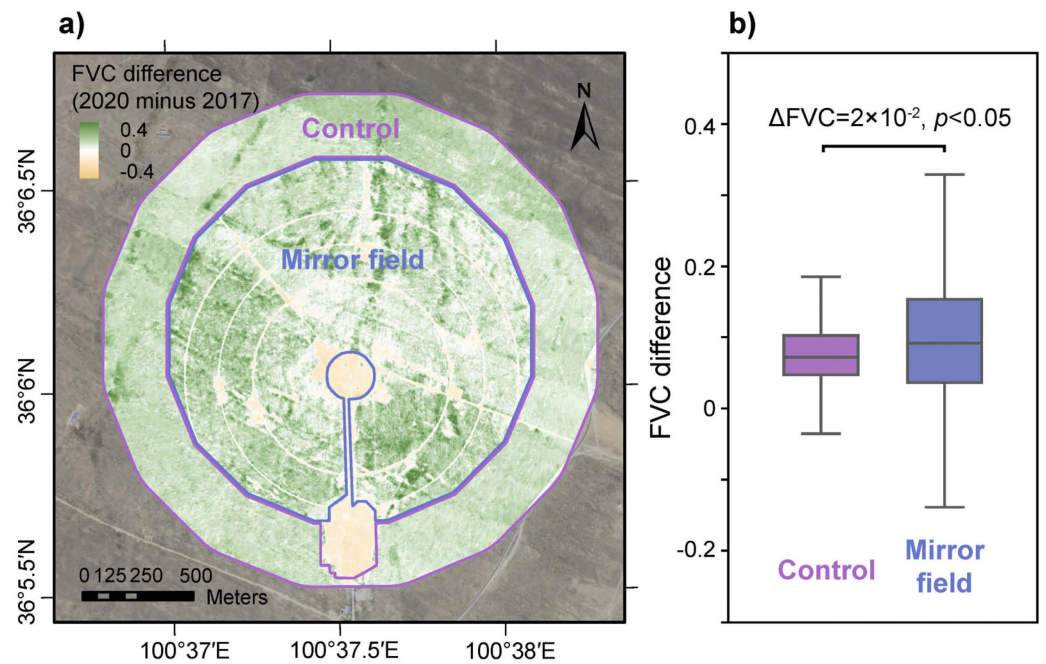


Figure 6. Spatial distribution of the FVC difference and ΔFVC of the Gonghe solar thermal power plant between 2017 and 2020. Subfigure (a) illustrates the spatial distribution of FVC differences along with the boundaries of the mirror field and control region. Subfigure (b) presents boxplots that depict the FVC differences observed in the mirror field and control region, with the ΔFVC values and the significance of the two-sample *t*-test detailed in the accompanying text.

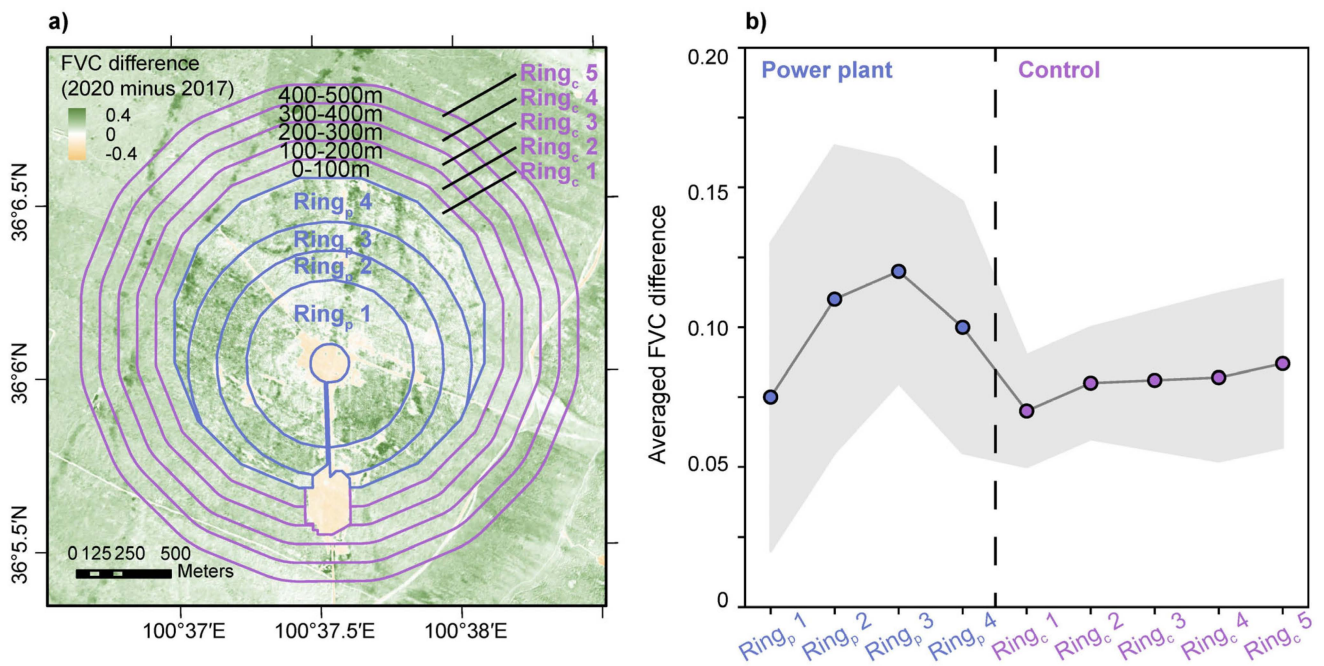


Figure 7. Distribution of the FVC difference of the Gonghe solar thermal power plant in the ring regions around the central tower and the power plant between 2017 and 2020. Subfigure (a) depicts the spatial arrangement of the rings, which include the power plant rings (Ring_p) and the control region rings (Ring_c). The control region rings are spaced at 100 m intervals, extending from 0 to 500 m beyond the boundaries of the Gonghe solar thermal power plant. Subfigure (b) illustrates the average FVC differences for each ring, with the standard deviations represented by the shaded area of the plot.

4. Discussion

4.1. The Impact of Solar Power Plants on Vegetation

Previous research has documented a 0.012 increase in the NDVI resulting from solar photovoltaic plants in arid and semi-arid regions of northern China [24], a figure significantly lower than the 0.02 increase in FVC reported in this study. Given the low baseline FVC of 0.16 in 2017, the Gonghe solar thermal power plant is associated with a 12.5% increase in FVC, which is believed to be considerably greater than the findings from arid regions in northern China. Several factors may contribute to this discrepancy. Firstly, the spatial resolution of the Landsat dataset used in studies of northern China is 30 m, which can lead to mixed pixel information encompassing both photovoltaic panels and the surrounding land surface [47]. This limitation may result in an underestimation of the vegetation dynamics associated with solar power installations. Secondly, it has been observed that solar photovoltaic plants in northern China can negatively impact vegetation when the background NDVI exceeds 0.6, potentially suppressing the average NDVI impact of these installations [24]. Thirdly, despite both technologies harnessing solar radiation for electricity generation, there is a key distinction between photovoltaic and solar thermal systems. Photovoltaic panels convert solar energy into electricity while simultaneously generating heat [20]. In contrast, solar thermal mirrors reflect solar radiation towards a central tower to heat molten salt, absorbing minimal radiation and producing little heat. The warming impact of photovoltaic panels might increase water stress and suppress vegetation growth in the arid zones in northern China [48].

There is evidence of vegetation decline associated with photovoltaic power plants on the southern Iberian Peninsula, attributed to soil moisture depletion caused by these installations [25]. The contrasting outcomes observed in China may be influenced by climatic differences between the two regions. The Iberian Peninsula experiences a Mediterranean climate characterized by winter precipitation and dry, hot conditions during the growing season [49], where the heat generated by photovoltaic panels may exacerbate drought conditions and inhibit vegetation growth. Additionally, the nighttime warming effect of these plants could further intensify water stress on the underlying flora [50,51]. In contrast, the East Asian monsoon brings moist air from the Pacific Ocean during the growing season, resulting in concurrent heat and precipitation in China [52], which may promote vegetation growth by reducing radiation exposure to the surface under the shade of photovoltaic panels.

The spatial distribution of FVC differences within the Gonghe solar thermal power plant reveals a significantly reduced FVC in the innermost ring surrounding the central tower when compared to the outer rings. This observation may be linked to the construction activities associated with the central facilities, as illustrated in Figure 6a. Furthermore, the spillover effects of the Gonghe solar thermal power plant on adjacent vegetation are not pronounced, as depicted in Figure 7b. Previous studies have documented the cooling effects of solar photovoltaic power plants on the Tibetan Plateau, indicating that such cooling effects diminish with increasing distance from the plant's boundary [15]. However, these spillover cooling effects do not appear to significantly influence the surrounding vegetation, potentially due to a complex interplay of factors such as the diurnal temperature range and local water conditions [50,53]. There is a need for further comprehensive observations of the climatic and ecological impacts associated with solar power plants.

To prove that the increase in FVC within the mirror field can be attributed primarily to the installation and operation of the Gonghe solar thermal power plant, it is essential to ensure that historical variations in FVC are comparable between the mirror field and the control region. Given the spatial extent of the Gonghe solar thermal power plant and the temporal scope of the pre-installation period, Landsat 7 imagery was utilized to assess FVC trends in both the mirror field and the control regions [54]. Specifically, images from June to August between 2010 and 2017 were selected, with a cloud cover threshold of less than 30% applied. Cloud and shadow masking algorithms were employed on the filtered images to enhance data quality. Subsequently, the NDVI was calculated using Equation (1), followed

by FVC estimation via Equation (4). A maximum composite approach was employed for the Landsat 7 FVC data annually from 2010 to 2017, allowing for the calculation of average FVC values in both the mirror field and control regions. All analytical procedures were conducted using GEE [36]. The results indicate that FVC trends in the mirror field and control regions were similar from 2010 to 2017; however, a divergence in these trends became apparent following the installation of the power plant (Figure S6). This suggests that the observed increase in FVC within the mirror field is predominantly influenced by the operational activities of the Gonghe solar thermal power plant.

4.2. Processes of Solar Power Plant Vegetation Impacts

The primary impact of solar power plants on local climate dynamics includes alterations to radiation, precipitation, and wind speed [12,55,56]. During the day, photovoltaic panels and solar thermal mirrors absorb or reflect incoming solar radiation, creating shaded areas that lower both land surface and near-surface air temperatures. This cooling effect can reduce surface evapotranspiration, thereby maintaining moisture levels [57]. Conversely, at night, these installations reflect upward longwave radiation, warming the surface and potentially enhancing ecosystem respiration [17]. Furthermore, photovoltaic panels and mirrors can modify precipitation patterns; they obstruct direct rainfall and snowfall from reaching the ground, while also influencing water erosion [58]. Additionally, by increasing surface roughness, solar power plants can decrease wind speed, which further mitigates wind erosion and reduces surface evapotranspiration [59]. Collectively, these factors can significantly influence local vegetation, depending on regional climatic conditions, vegetation types, and levels of human management [60,61].

In this study, the Gonghe solar thermal power plant was associated with a 0.02 increase in FVC compared to adjacent control regions, reflecting a 12.5% increase relative to the baseline FVC. Notably, the control region itself also exhibited a 0.07 increase in FVC from 2017 to 2020. This change may be attributed to a reduction in climate-related water stress. As illustrated in Figure S7, annual precipitation increased significantly by 9.33 mm per year ($p < 0.01$), while annual potential evaporation decreased by 13.19 mm per year from 2010 to 2020 ($p < 0.01$). These trends indicate improved hydrological conditions conducive to vegetation growth [62]. Specifically, during the peak growing season (May to August), precipitation levels were 47 mm higher in 2020 compared to 2017, while potential evaporation was 74 mm lower, translating to an 18% increase in rainfall and an 11% decrease in potential evaporation. To strengthen the analysis, we incorporated an alternative climate dataset with a spatial resolution of 1 km [63]. The results indicate that precipitation and potential evaporation trends closely mirror those observed in the ERA5-Land dataset, with significant increases in annual precipitation and decreases in potential evaporation at $p < 0.01$ (Figure S8). These changes likely contributed to the enhanced FVC observed in the control region surrounding the Gonghe solar thermal power plant. Furthermore, the reflecting mirrors of the power plant provide shade that further reduces surface temperature evaporation, alleviating water stress and promoting photosynthesis among vegetation in the semi-arid environment of the Tibetan Plateau [15,64]. Additionally, human management practices, including the washing of the mirrors, introduced supplemental water to the mirror field, further improving the hydrological conditions and vegetation growth of the power plant [65].

Long-term observations from meteorological stations have elucidated the climatic effects of solar power plants. Specifically, the shading provided by solar panels has been shown to decrease incident radiation by 2.5 megajoules $m^{-2} h^{-1}$. Furthermore, solar panels can lower the soil temperature at a depth of 5 cm by 10.9 °C during the day, suggesting a concomitant reduction in evapotranspiration attributable to the panels' shading effects [66,67]. Additionally, as photovoltaic panels convert solar radiation into electricity, they generate heat that warms the surrounding air. In the absence of this conversion process, it is reasonable to postulate that the air temperature near solar thermal reflecting mirrors would be cooler, thereby alleviating water stress on adjacent vegetation [20,48].

4.3. Limitation and Future Work

In this study, we evaluate the Δ FVC associated with the Gonghe solar thermal power plant using sub-meter resolution satellite imagery from GF-2, captured in 2017 and 2020. However, several limitations affect our analysis. Firstly, the high spatial resolution of the GF-2 imagery restricts the scene size, which in turn limits the revisit frequency for specific locations. After filtering the GF-2 images based on geolocation and cloud cover, we identified only two suitable images from the peak growing seasons between 2017 and 2024 for this analysis. The coarse temporal resolution, both inter-annually and monthly, constrains our ability to thoroughly examine the impact of the power plant on phenology and post-installation vegetation dynamics [68]. Secondly, the multispectral bands available from the GF-2 imagery are limited to near-infrared, red, green, and blue, in contrast to the eight bands of Landsat 8 and twelve bands of Sentinel-2 satellites [69]. This limitation in spectral information reduces the potential for detailed applications of the GF-2 data, such as the classification of more nuanced land cover types. Thirdly, while the post-installation imagery for this study was collected in 2020, our in situ sampling occurred in 2024, as no suitable imagery was available from 2021 to 2024. This temporal gap may introduce bias in the reconstruction of the FVC for 2020, and we were unable to predict the availability of suitable imagery prior to conducting the in situ sampling. The integration of multisource data may offer a potential solution to this challenge.

Unmanned aerial vehicles (UAVs) are increasingly employed in regional ground monitoring [70]. However, two critical considerations must be addressed when utilizing UAVs to study solar thermal power plants. First, the reflecting mirrors adjust their rotation and pitch according to the sun's position [71], necessitating careful design of the UAV's camera angle and flight path to effectively capture information beneath the mirrors. Second, the mirrors concentrate solar radiation toward the central tower, creating the potential for heat damage to the UAV in adjacent areas [72]. Consequently, the UAV's flight route should be planned to avoid these high-temperature zones.

While the GF-2 data and methodologies employed in this study provide more precise results than those derived from coarser-resolution remote sensing images, the constraints of limited spatial coverage and temporal resolution hinder comprehensive analysis. The approach utilized here could also be applied to assess the impacts of photovoltaic power plants, enabling spatial and temporal extension of solar energy studies. This would allow for an exploration of spatial heterogeneity in impacts and a deeper investigation into influencing factors. We employed 174 in situ samples to reconstruct the FVC, a process that could be enhanced through the use of UAV remote sensing for greater sampling efficiency [73]. The UAV capabilities allow for improved temporal resolution of observations concerning the Gonghe solar thermal power plant, both inter-annually and within a single growing season. Such continuous inter-annual time series data would enhance the accuracy of our analyses and facilitate further investigations into aspects such as vegetation phenology [74]. By integrating continuous observations from satellites, UAVs, and in situ measurements at solar energy facilities, we can conduct more accurate analyses of climate and ecological impacts, leading to a deeper understanding of the underlying mechanisms. Furthermore, given the rapid advancement in solar energy development, it is critical to assess the climate and ecological impacts prior to construction. Adequate observational data are necessary to develop and validate climate models, such as the Weather Research and Forecasting (WRF) model or statistical models [12]. Utilizing these models will enable us to evaluate the climate and ecological effects of solar energy facilities, thereby ensuring environmental safety and the sustainable generation of clean energy in the near future.

5. Conclusions

In this study, we evaluate the influence of the Gonghe solar thermal power plant on FVC utilizing GF-2 imagery, employing methods such as soft voting classification, in situ sampling, and image reconstruction. Our findings indicate that the average FVC beneath the solar mirrors is 1.36 times greater than that of adjacent uncovered areas. The power

plant is associated with a 0.02 increase in FVC relative to surrounding control regions, representing a 12.5% enhancement compared to the pre-construction phase. Notably, the increase in FVC is more pronounced in the outer ring areas than in proximity to the central tower. This research introduces a novel methodology for more accurately assessing the impacts of not only solar thermal power plants, but also photovoltaic installations. By examining the effects of solar power plants on local vegetation, we can facilitate the harmonious co-development of local ecosystems alongside clean energy generation.

Supplementary Materials: The following supporting information can be downloaded at: <https://www.mdpi.com/article/10.3390/rs16224266/s1>, Figure S1. In-situ sample pairs at the Gonghe solar thermal power plant. Figure S2. Training and validation samples for soft voting classification method in this study. Figure S3. Assessment of GF-2 FVC through in-situ sampling. Figure S4. FVC ratio between surfaces under and between mirrors of the Gonghe solar thermal power plant. Figure S5. Boxplot illustrating the differences in grassland FVC between the mirror field and the control region. Figure S6. Time series of FVC from Landsat 7 and GF-2 spanning the years 2010 to 2020. Figure S7. Time series of ERA5 Land precipitation and potential evaporation of the Gonghe solar thermal power plant. Figure S8. Time series of 1-kilometer precipitation and potential evaporation of the Gonghe solar thermal power plant.

Author Contributions: Conceptualization, N.L. and Y.L.; methodology, N.L. and H.P.; validation, Z.Z., K.Z., and D.W.; formal analysis, N.L.; investigation, Y.G. and Y.C.; data curation, Y.G. and Y.C.; writing—original draft preparation, N.L.; writing—review and editing, Y.J. and W.G.; visualization, N.L. and D.W.; funding acquisition, H.P. All authors have read and agreed to the published version of the manuscript.

Funding: This research was funded by the National Key R&D Program of China (2022YFB4202100), “Young Top-notch Talent” in Pearl River talent plan of Guangdong Province, China (grant number 2023QN10L248).

Data Availability Statement: The raw data supporting the conclusions of this article will be made available by the authors on request.

Conflicts of Interest: Authors Naijing Liu, Huaiwu Peng, Zhenshi Zhang, Yujin Li, Yuehan Guo, Yingsha Jiang, Wenxiang Gao were employed by the company POWERCHINA Northwest Engineering Corporation Limited. The remaining authors declare that the research was conducted in the absence of any commercial or financial relationships that could be construed as a potential conflict of interest.

References

1. Davis, S.J.; Lewis, N.S.; Shaner, M.; Aggarwal, S.; Arent, D.; Azevedo, I.L.; Benson, S.M.; Bradley, T.; Brouwer, J.; Chiang, Y.-M.; et al. Net-Zero Emissions Energy Systems. *Science* **2018**, *360*, eaas9793. [[CrossRef](#)] [[PubMed](#)]
2. Ember Yearly Electricity Data 2024. Available online: <https://ember-energy.org/data/yearly-electricity-data/> (accessed on 12 November 2024).
3. Liu, Z.; Guan, D.; Moore, S.; Lee, H.; Su, J.; Zhang, Q. Climate Policy: Steps to China’s Carbon Peak. *Nature* **2015**, *522*, 279–281. [[CrossRef](#)] [[PubMed](#)]
4. Zhang, D.; Wang, J.; Lin, Y.; Si, Y.; Huang, C.; Yang, J.; Huang, B.; Li, W. Present Situation and Future Prospect of Renewable Energy in China. *Renew. Sustain. Energy Rev.* **2017**, *76*, 865–871. [[CrossRef](#)]
5. Liu, L.; Wang, Z.; Wang, Y.; Wang, J.; Chang, R.; He, G.; Tang, W.; Gao, Z.; Li, J.; Liu, C.; et al. Optimizing Wind/Solar Combinations at Finer Scales to Mitigate Renewable Energy Variability in China. *Renew. Sustain. Energy Rev.* **2020**, *132*, 110151. [[CrossRef](#)]
6. Tian, Y.; Zhao, C.Y. A Review of Solar Collectors and Thermal Energy Storage in Solar Thermal Applications. *Appl. Energy* **2013**, *104*, 538–553. [[CrossRef](#)]
7. Palacios, A.; Barreneche, C.; Navarro, M.E.; Ding, Y. Thermal Energy Storage Technologies for Concentrated Solar Power—A Review from a Materials Perspective. *Renew. Energy* **2020**, *156*, 1244–1265. [[CrossRef](#)]
8. Weiss, W.; Spörk-Dür, M. *Solar Heat Worldwide 2024*; Institute for Sustainable Technologies: Gleisdorf, Austria, 2024.
9. Li, Y.; Kalnay, E.; Motescharrei, S.; Rivas, J.; Kucharski, F.; Kirk-Davidoff, D.; Bach, E.; Zeng, N. Climate Model Shows Large-Scale Wind and Solar Farms in the Sahara Increase Rain and Vegetation. *Science* **2018**, *361*, 1019–1022. [[CrossRef](#)]
10. McKuin, B.; Zumkehr, A.; Ta, J.; Bales, R.; Viers, J.H.; Pathak, T.; Campbell, J.E. Energy and Water Co-Benefits from Covering Canals with Solar Panels. *Nat. Sustain.* **2021**, *4*, 609–617. [[CrossRef](#)]

11. Kannenberg, S.A.; Sturchio, M.A.; Venturas, M.D.; Knapp, A.K. Grassland Carbon-Water Cycling Is Minimally Impacted by a Photovoltaic Array. *Commun. Earth Environ.* **2023**, *4*, 238. [[CrossRef](#)]
12. Chang, R.; Luo, Y.; Zhu, R. Simulated Local Climatic Impacts of Large-Scale Photovoltaics over the Barren Area of Qinghai, China. *Renew. Energy* **2020**, *145*, 478–489. [[CrossRef](#)]
13. Armstrong, A.; Waldron, S.; Whitaker, J.; Ostle, N.J. Wind Farm and Solar Park Effects on Plant-Soil Carbon Cycling: Uncertain Impacts of Changes in Ground-Level Microclimate. *Glob. Chang. Biol.* **2014**, *20*, 1699–1706. [[CrossRef](#)] [[PubMed](#)]
14. Fan, C.; Huang, X. Satellite-Observed Changes of Surface Spectral Reflectances Due to Solar Farming and the Implication for Radiation Budget. *Environ. Res. Lett.* **2020**, *15*, 114047. [[CrossRef](#)]
15. Li, G.; Hernandez, R.R.; Blackburn, G.A.; Davies, G.; Hunt, M.; Whyatt, J.D.; Armstrong, A. Ground-Mounted Photovoltaic Solar Parks Promote Land Surface Cool Islands in Arid Ecosystems. *Renew. Sustain. Energy Transit.* **2021**, *1*, 100008.
16. Zhang, X.; Xu, M. Assessing the Effects of Photovoltaic Powerplants on Surface Temperature Using Remote Sensing Techniques. *Remote Sens.* **2020**, *12*, 1825. [[CrossRef](#)]
17. Li, Z.; Zhao, Y.; Luo, Y.; Yang, L.; Li, P.; Jin, X.; Jiang, J.; Liu, R.; Gao, X. A Comparative Study on the Surface Radiation Characteristics of Photovoltaic Power Plant in the Gobi Desert. *Renew. Energy* **2022**, *182*, 764–771. [[CrossRef](#)]
18. Xu, Z.; Li, Y.; Qin, Y.; Bach, E. A Global Assessment of the Effects of Solar Farms on Albedo, Vegetation, and Land Surface Temperature Using Remote Sensing. *Sol. Energy* **2024**, *268*, 112198. [[CrossRef](#)]
19. Barron-Gafford, G.A.; Minor, R.L.; Allen, N.A.; Cronin, A.D.; Brooks, A.E.; Pavao-Zuckerman, M.A. The Photovoltaic Heat Island Effect: Larger Solar Power Plants Increase Local Temperatures. *Sci. Rep.* **2016**, *6*, 35070. [[CrossRef](#)]
20. Hu, M.; Zhao, B.; Suhendri, A.; Ao, X.; Cao, J.; Wang, Q.; Riffat, S.; Su, Y.; Pei, G. Applications of Radiative Sky Cooling in Solar Energy Systems: Progress, Challenges, and Prospects. *Renew. Sustain. Energy Rev.* **2022**, *160*, 112304. [[CrossRef](#)]
21. Lu, Z.; Zhang, Q.; Miller, P.A.; Zhang, Q.; Berntell, E.; Smith, B. Impacts of Large-Scale Sahara Solar Farms on Global Climate and Vegetation Cover. *Geophys. Res. Lett.* **2021**, *48*, e2020GL090789. [[CrossRef](#)]
22. Zhao, W.; Zhao, J.; Liu, M.; Gao, Y.; Li, W.; Duan, H. Vegetation Restoration Increases Soil Carbon Storage in Land Disturbed by a Photovoltaic Power Station in Semi-Arid Regions of Northern China. *Agronomy* **2024**, *14*, 9. [[CrossRef](#)]
23. Xia, Z.; Li, Y.; Zhang, W.; Guo, S.; Zheng, L.; Jia, N.; Chen, R.; Guo, X.; Du, P. Quantitatively Distinguishing the Impact of Solar Photovoltaics Programs on Vegetation in Dryland Using Satellite Imagery. *Land Degrad. Dev.* **2023**, *34*, 4373–4385. [[CrossRef](#)]
24. Xia, Z.; Li, Y.; Guo, S.; Chen, R.; Zhang, W.; Guo, X.; Zhang, X.; Du, P. Satellites Reveal Spatial Heterogeneity in Dryland Photovoltaic Plants' Effects on Vegetation Dynamics. *Earths Future* **2024**, *12*, e2024EF004427. [[CrossRef](#)]
25. Muñoz-García, M.-Á.; Fialho, L.; Moreda, G.P.; Baptista, F. Assessment of the Impact of Utility-Scale Photovoltaics on the Surrounding Environment in the Iberian Peninsula. Alternatives for the Coexistence with Agriculture. *Sol. Energy* **2024**, *271*, 112446. [[CrossRef](#)]
26. Appelbaum, J.; Aronescu, A. Inter-Row Spacing Calculation in Photovoltaic Fields—A New Approach. *Renew. Energy* **2022**, *200*, 387–394. [[CrossRef](#)]
27. Ma, C.; Deng, Z.; Xu, X.; Pang, X.; Li, X.; Wu, R.; Tian, Z. Space Optimization of Utility-Scale Photovoltaic Power Plants Considering the Impact of Inter-Row Shading. *Appl. Energy* **2024**, *370*, 123591. [[CrossRef](#)]
28. Biskaborn, B.K.; Smith, S.L.; Noetzi, J.; Matthes, H.; Vieira, G.; Streletskiy, D.A.; Schoeneich, P.; Romanovsky, V.E.; Lewkowicz, A.G.; Abramov, A.; et al. Permafrost Is Warming at a Global Scale. *Nat. Commun.* **2019**, *10*, 264. [[CrossRef](#)]
29. Wu, G.; Duan, A.; Liu, Y.; Mao, J.; Ren, R.; Bao, Q.; He, B.; Liu, B.; Hu, W. Tibetan Plateau Climate Dynamics: Recent Research Progress and Outlook. *Natl. Sci. Rev.* **2015**, *2*, 100–116. [[CrossRef](#)]
30. Fang, Y.; Wei, Y. Climate Change Adaptation on the Qinghai–Tibetan Plateau: The Importance of Solar Energy Utilization for Rural Household. *Renew. Sustain. Energy Rev.* **2013**, *18*, 508–518. [[CrossRef](#)]
31. Yang, X.; Xie, F.; Liu, S.; Zhu, Y.; Fan, J.; Zhao, H.; Fu, Y.; Duan, Y.; Fu, R.; Guo, S. Mapping Debris-Covered Glaciers Using High-Resolution Imagery (GF-2) and Deep Learning Algorithms. *Remote Sens.* **2024**, *16*, 2062. [[CrossRef](#)]
32. He, Q.; Sun, X.; Yan, Z.; Fu, K. DABNet: Deformable Contextual and Boundary-Weighted Network for Cloud Detection in Remote Sensing Images. *IEEE Trans. Geosci. Remote Sens.* **2022**, *60*, 5601216. [[CrossRef](#)]
33. Cooley, T.; Anderson, G.P.; Felde, G.W.; Hoke, M.L.; Ratkowski, A.J.; Chetwynd, J.H.; Gardner, J.A.; Adler-Golden, S.M.; Matthew, M.W.; Berk, A.; et al. FLAASH, a MODTRAN4-Based Atmospheric Correction Algorithm, Its Application and Validation. In Proceedings of the IGARSS 2002: International Geoscience and Remote Sensing Symposium, 24th Canadian Symposium on Remote Sensing, Toronto, ON, Canada, 24–28 June 2002; IEEE: New York, NY, USA, 2002; pp. 1414–1418.
34. Sun, W.; Chen, B.; Messinger, D.W. Nearest-Neighbor Diffusion-Based Pan-Sharpener Algorithm for Spectral Images. *Opt. Eng.* **2014**, *53*, 013107. [[CrossRef](#)]
35. Muñoz-Sabater, J.; Dutra, E.; Agustí-Panareda, A.; Albergel, C.; Arduini, G.; Balsamo, G.; Boussetta, S.; Choulga, M.; Harrigan, S.; Hersbach, H.; et al. ERA5-Land: A State-of-the-Art Global Reanalysis Dataset for Land Applications. *Earth Syst. Sci. Data* **2021**, *13*, 4349–4383. [[CrossRef](#)]
36. Gorelick, N.; Hancher, M.; Dixon, M.; Ilyushchenko, S.; Thau, D.; Moore, R. Google Earth Engine: Planetary-Scale Geospatial Analysis for Everyone. *Remote Sens. Environ.* **2017**, *202*, 18–27. [[CrossRef](#)]
37. Gandhi, I.; Pandey, M. Hybrid Ensemble of Classifiers Using Voting. In Proceedings of the 2015 International Conference on Green Computing and Internet of Things (ICGCIoT), Delhi, India, 8–10 October 2015; pp. 399–404.
38. Breiman, L. Random Forests. *Mach. Learn.* **2001**, *45*, 5–32. [[CrossRef](#)]

39. Pisner, D.A.; Schnyer, D.M. Support Vector Machine. In *Machine Learning*; Elsevier: Amsterdam, The Netherlands, 2020; pp. 101–121.
40. Peterson, L.E. K-Nearest Neighbor. *Scholarpedia* **2009**, *4*, 1883. [[CrossRef](#)]
41. Pedregosa, F.; Varoquaux, G.; Gramfort, A.; Michel, V.; Thirion, B.; Grisel, O.; Blondel, M.; Prettenhofer, P.; Weiss, R.; Dubourg, V.; et al. Scikit-Learn: Machine Learning in Python. *J. Mach. Learn. Res.* **2011**, *12*, 2825–2830.
42. Castillo-Martínez, M.Á.; Gallegos-Funes, F.J.; Carvajal-Gámez, B.E.; Urriolagoitia-Sosa, G.; Rosales-Silva, A.J. Color Index Based Thresholding Method for Background and Foreground Segmentation of Plant Images. *Comput. Electron. Agric.* **2020**, *178*, 105783. [[CrossRef](#)]
43. Hamuda, E.; Glavin, M.; Jones, E. A Survey of Image Processing Techniques for Plant Extraction and Segmentation in the Field. *Comput. Electron. Agric.* **2016**, *125*, 184–199. [[CrossRef](#)]
44. Lu, G.Y.; Wong, D.W. An Adaptive Inverse-Distance Weighting Spatial Interpolation Technique. *Comput. Geosci.* **2008**, *34*, 1044–1055. [[CrossRef](#)]
45. Babu, S.C.; Gajanan, S.N. Chapter 16-Food and Nutrition Program Evaluation. In *Food Security, Poverty and Nutrition Policy Analysis*, 3rd ed.; Babu, S.C., Gajanan, S.N., Eds.; Academic Press: San Diego, CA, USA, 2022; pp. 575–597. ISBN 978-0-12-820477-1.
46. Liu, N.; Zhao, X.; Zhang, X.; Zhao, J.; Wang, H.; Wu, D. Remotely Sensed Evidence of the Divergent Climate Impacts of Wind Farms on Croplands and Grasslands. *Sci. Total Environ.* **2023**, *905*, 167203. [[CrossRef](#)]
47. Ling, F.; Du, Y.; Xiao, F.; Li, X. Subpixel Land Cover Mapping by Integrating Spectral and Spatial Information of Remotely Sensed Imagery. *IEEE Geosci. Remote. Sens. Lett.* **2012**, *9*, 408–412. [[CrossRef](#)]
48. Grossiord, C.; Buckley, T.N.; Cernusak, L.A.; Novick, K.A.; Poulter, B.; Siegwolf, R.T.; Sperry, J.S.; McDowell, N.G. Plant Responses to Rising Vapor Pressure Deficit. *New Phytol.* **2020**, *226*, 1550–1566. [[CrossRef](#)] [[PubMed](#)]
49. Peel, M.C.; Finlayson, B.L.; McMahon, T.A. Updated World Map of the Köppen-Geiger Climate Classification. *Hydrol. Earth Syst. Sci.* **2007**, *11*, 1633–1644. [[CrossRef](#)]
50. Fu, Y.; Yu, G.; Wang, Y.; Li, Z.; Hao, Y. Effect of Water Stress on Ecosystem Photosynthesis and Respiration of a *Leymus Chinensis* Steppe in Inner Mongolia. *Sci. China Earth Sci.* **2006**, *49*, 196. [[CrossRef](#)]
51. Wu, D.; Grodsky, S.M.; Xu, W.; Liu, N.; Almeida, R.M.; Zhou, L.; Miller, L.M.; Roy, S.B.; Xia, G.; Agrawal, A.A.; et al. Observed Impacts of Large Wind Farms on Grassland Carbon Cycling. *Sci. Bull.* **2023**, *68*, 2889–2892. [[CrossRef](#)]
52. Wang, B.; Biasutti, M.; Byrne, M.P.; Castro, C.; Chang, C.-P.; Cook, K.; Fu, R.; Grimm, A.M.; Ha, K.-J.; Hendon, H.; et al. Monsoons Climate Change Assessment. *Bull. Am. Meteorol. Soc.* **2021**, *102*, E1–E19. [[CrossRef](#)]
53. Peng, S.; Piao, S.; Ciais, P.; Myneni, R.B.; Chen, A.; Chevallier, F.; Dolman, A.J.; Janssens, I.A.; Peñuelas, J.; Zhang, G.; et al. Asymmetric Effects of Daytime and Night-Time Warming on Northern Hemisphere Vegetation. *Nature* **2013**, *501*, 88–92. [[CrossRef](#)]
54. Lewińska, K.E.; Buchner, J.; Bleyhl, B.; Hostert, P.; Yin, H.; Kuemmerle, T.; Radeloff, V.C. Changes in the Grasslands of the Caucasus Based on Cumulative Endmember Fractions from the Full 1987–2019 Landsat Record. *Sci. Remote Sens.* **2021**, *4*, 100035. [[CrossRef](#)]
55. Nguyen, K.C.; Katzfey, J.J.; Riedl, J.; Troccoli, A. Potential Impacts of Solar Arrays on Regional Climate and on Array Efficiency. *Int. J. Climatol.* **2017**, *37*, 4053–4064. [[CrossRef](#)]
56. Broadbent, A.M.; Krayenhoff, E.S.; Georgescu, M.; Sailor, D.J. The Observed Effects of Utility-Scale Photovoltaics on Near-Surface Air Temperature and Energy Balance. *J. Appl. Meteorol. Climatol.* **2019**, *58*, 989–1006. [[CrossRef](#)]
57. Wu, C.; Liu, H.; Yu, Y.; Zhao, W.; Liu, J.; Yu, H.; Yetemen, O. Ecohydrological Effects of Photovoltaic Solar Farms on Soil Microclimates and Moisture Regimes in Arid Northwest China: A Modeling Study. *Sci. Total Environ.* **2022**, *802*, 149946. [[CrossRef](#)] [[PubMed](#)]
58. Liu, H.; Wu, C.; Yu, Y.; Zhao, W.; Liu, J.; Yu, H.; Zhuang, Y.; Yetemen, O. Effect of Solar Farms on Soil Erosion in Hilly Environments: A Modeling Study From the Perspective of Hydrological Connectivity. *Water Resour. Res.* **2023**, *59*, e2023WR035067. [[CrossRef](#)]
59. Liu, Z.; Ma, C.; Yang, Y.; Li, X.; Gou, H.; Folkard, A.M. Water Temperature and Energy Balance of Floating Photovoltaic Construction Water Area—Field Study and Modelling. *J. Environ. Manag.* **2024**, *365*, 121494. [[CrossRef](#)] [[PubMed](#)]
60. Power, K.; Lu, Z.; Zhang, Q. Impacts of Large-Scale Saharan Solar Farms on the Global Terrestrial Carbon Cycle. *Environ. Res. Lett.* **2023**, *18*, 104009. [[CrossRef](#)]
61. Wang, Y.; Liu, B.; Xing, Y.; Peng, H.; Wu, H.; Zhong, J. Ecological Construction Status of Photovoltaic Power Plants in China’s Deserts. *Front. Environ. Sci.* **2024**, *12*, 1406546. [[CrossRef](#)]
62. Zhu, Z.; Piao, S.; Myneni, R.B.; Huang, M.; Zeng, Z.; Canadell, J.G.; Ciais, P.; Sitch, S.; Friedlingstein, P.; Arneeth, A.; et al. Greening of the Earth and Its Drivers. *Nat. Clim. Chang.* **2016**, *6*, 791–795. [[CrossRef](#)]
63. Peng, S.; Ding, Y.; Liu, W.; Li, Z. 1 Km Monthly Temperature and Precipitation Dataset for China from 1901 to 2017. *Earth Syst. Sci. Data* **2019**, *11*, 1931–1946. [[CrossRef](#)]
64. Huang, Y.; Xin, Z.; Dor-ji, T.; Wang, Y. Tibetan Plateau Greening Driven by Warming-Wetting Climate Change and Ecological Restoration in the 21st Century. *Land Degrad. Dev.* **2022**, *33*, 2407–2422. [[CrossRef](#)]
65. García-Segura, A.; Sutter, F.; Martínez-Arcos, L.; Reche-Navarro, T.J.; Wiesinger, F.; Wette, J.; Buendía-Martínez, F.; Fernández-García, A. Degradation Types of Reflector Materials Used in Concentrating Solar Thermal Systems. *Renew. Sustain. Energy Rev.* **2021**, *143*, 110879. [[CrossRef](#)]
66. Marrou, H.; Guillioni, L.; Dufour, L.; Dupraz, C.; Wery, J. Microclimate under Agrivoltaic Systems: Is Crop Growth Rate Affected in the Partial Shade of Solar Panels? *Agric. For. Meteorol.* **2013**, *177*, 117–132. [[CrossRef](#)]

67. Yang, L.; Gao, X.; Lv, F.; Hui, X.; Ma, L.; Hou, X. Study on the Local Climatic Effects of Large Photovoltaic Solar Farms in Desert Areas. *Sol. Energy* **2017**, *144*, 244–253. [[CrossRef](#)]
68. Zhang, J.; Xiao, J.; Tong, X.; Zhang, J.; Meng, P.; Li, J.; Liu, P.; Yu, P. NIRv and SIF Better Estimate Phenology than NDVI and EVI: Effects of Spring and Autumn Phenology on Ecosystem Production of Planted Forests. *Agric. For. Meteorol.* **2022**, *315*, 108819. [[CrossRef](#)]
69. Drusch, M.; Del Bello, U.; Carlier, S.; Colin, O.; Fernandez, V.; Gascon, F.; Hoersch, B.; Isola, C.; Laberinti, P.; Martimort, P.; et al. Sentinel-2: ESA's Optical High-Resolution Mission for GMES Operational Services. *Remote Sens. Environ.* **2012**, *120*, 25–36. [[CrossRef](#)]
70. Lyu, X.; Li, X.; Dang, D.; Dou, H.; Wang, K.; Lou, A. Unmanned Aerial Vehicle (UAV) Remote Sensing in Grassland Ecosystem Monitoring: A Systematic Review. *Remote Sens.* **2022**, *14*, 1096. [[CrossRef](#)]
71. Kurkute, N.; Priyam, A. A Thorough Review of the Existing Concentrated Solar Power Technologies and Various Performance Enhancing Techniques. *J. Therm. Anal. Calorim.* **2022**, *147*, 14713–14737. [[CrossRef](#)]
72. Qin, J.; Hu, E.; Nathan, G.J.; Chen, L. Concentrating or Non-Concentrating Solar Collectors for Solar Aided Power Generation? *Energy Convers. Manag.* **2017**, *152*, 281–290. [[CrossRef](#)]
73. Maimaitijiang, M.; Sagan, V.; Sidike, P.; Daloye, A.M.; Erkbol, H.; Fritschi, F.B. Crop Monitoring Using Satellite/UAV Data Fusion and Machine Learning. *Remote Sens.* **2020**, *12*, 1357. [[CrossRef](#)]
74. Liu, Z.; Li, G.; Wang, G. Can Wind Farms Change the Phenology of Grassland in China? *Sci. Total Environ.* **2022**, *832*, 155077. [[CrossRef](#)]

Disclaimer/Publisher's Note: The statements, opinions and data contained in all publications are solely those of the individual author(s) and contributor(s) and not of MDPI and/or the editor(s). MDPI and/or the editor(s) disclaim responsibility for any injury to people or property resulting from any ideas, methods, instructions or products referred to in the content.